Proceedings of DETC'05
ASME 2005 Design Engineering Technical Conferences and Computers and Information in Engineering Conference
Long Beach, California, September 24-28, 2005

DETC2005/ DAC-84768

CONTINUUM-BASED DESIGN SENSITIVITY ANALYSIS AND OPTIMIZATION OF SPRINGBACK IN STAMPING PROCESS

Kyung K. Choi and Kiyoung Yi
Center for Computer-Aided Design and
Department of Mechanical & Industrial Engineering
The University of Iowa
Iowa City, IA 52242, USA
kkchoi@ccad.uiowa.edu, kyyi@ccad.uiowa.edu

Nam H. Kim
Department of Mechanical & Aerospace Engineering
College of Engineering
University of Florida
Gainesville, FL32611, USA
nkim@ufl.edu

Mark E. Botkin
Vehicle Analysis & Dynamics
General Motors R&D and Planning
Mail Code 480–106–256
30500 Mound Rd. 106
Box 9055
Warren, MI 48090–9055
mark_e._botkin@gmr.com

ABSTRACT

The springback is a significant manufacturing defect in the stamping process. A serious impediment to the use of lighter-weight, higher-strength materials in manufacturing is the relative lack of understanding about how these materials respond to the complex forming process. The springback problem can be reduced by using appropriate designs of die, punch, and blank holder shape together with friction and blank holding force. That is, an optimum stamping process can be determined using a gradient-based optimization to minimize the springback. However, for an effective optimization of the stamping process, development of an efficient analytical design sensitivity analysis method is crucial. In this paper, a continuum-based shape and configuration design sensitivity analysis (DSA) method for the stamping process has been developed. The material derivative concept is used to develop the continuum-based design sensitivity. The design sensitivity equation is solved without iteration at each converged load step in the finite deformation elastoplastic nonlinear analysis with frictional contact, which makes the design sensitivity calculation very efficient. The accuracy and efficiency of the proposed method is illustrated by minimizing springback in an S-rail part, which is often used as an industrial benchmark to verify the numerical procedures employed for stamping processes.

KEYWORDS

Stamping Process, Springback, Finite Deformation Elastoplasticity, Frictional Contact, Design Sensitivity Analysis, Design Optimization

1. INTRODUCTION

The stamping process was a major industrial breakthrough that made mass production of various products, which range from automobiles to home appliances, possible. However, springback in metal stamping is still very much problematic such that it requires a trial-and-error process to remove it, which is very expensive. For example, a large size die for a passenger vehicle side door could cost up to one million dollars. These days, carmakers face ever more frequently the phenomenon of springback, especially with new high strength steels. As a result, industries need a better understanding of how to compensate for springback in the stamping process especially for lightweight materials like aluminum and high strength steel.

The stamping process involves a combination of elastoplastic bending and stretching deformation of the blank sheet through frictional contact. These deformations can lead to large amounts of springback after the punch, die, blank holder are removed. The springback behavior is very complex and is affected by many factors including material properties, clearance between punch and die, thickness of the blank sheet, the tool (die, punch, and blank holder) shape, and blank holding force. Simulation of such behaviors using numerical methods such as FEA is still very much challenging problem, let alone design sensitivity analysis (DSA). Thus, extensive research efforts on the simulation of stamping process have been reported in several journals and conferences such as NUMISHEET [1-6].

There have been several attempts to reduce the springback problem. For example, Wenner [7] showed that tensile stretching stresses superimposed on the bending stresses of an elastoplastic material could reduce the springback in two-dimensional formed parts. Liu [8] has proposed variations of the blank holding force during the forming process to provide tensile pre-loading or post-loading on the formed part for springback reduction. However, it is not always possible to transmit high tensile forces to all parts of a blank sheet with complicated geometry without causing failure by tearing of the formed part. Karafillis and Boyce [9] proposed a methodology for tool shape design based on the inverse springback calculation. In their method, the traction distribution on the formed part is calculated at the fully loaded stage and this traction distribution was used to elastically load a part to give the desired die shape. However, these methods cannot be easily applied to the stamping process of complex formed part shape.

In recent years, DSA has been used for the stamping process design [10-12]. As it is pointed out by Choi *et al.* [13], there are three approaches for DSA: the finite difference method (FDM), discrete method, and continuum-based method. Among them, the continuum-based method differentiates the variational equation before discretization and thus is more efficient and accurate than the two other methods, although it requires lengthy and sophisticated mathematical derivations. In this paper, a continuum-based DSA method for a stamping process has been developed. The DSA for the stamping process is quite challenging because it requires sensitivity analysis of a shell structure with three nonlinearities: elastoplasticity, finite deformation, and frictional contact. Detailed discussion of DSA for a finite deformation elastoplastic shell structure is developed by Choi *et al*. [13], where the continuum-based DSA method is developed using the elastoplastic return-mapping algorithm [14] along with the Hughes-Winget's incrementally objective integration algorithm [15-17].

By integrating the DSA results of Ref. 7 and the newly developed DSA method for the frictional contact problem in this paper, a continuum-based DSA method for a finite deformation elastoplastic nonlinear shell structure with frictional contact is developed. For the frictional contact problem, instead of the contact variational inequality, a penalty-regularized variational equation is differentiated with respect to the stamping process parameters. The material derivative that is consistent with the frictional return-mapping scheme is derived. A piecewise-linear contact surface causes a significant amount of difficulty in the Newton-type iterative method because it lacks continuity across the surface boundary. CAD geometric representations of die and punch surfaces alleviates that difficulty significantly by providing smooth contact surface.

For DSA of the stamping process, the sensitivity equation uses the same tangent stiffness matrix as the response analysis, which is already decomposed during nonlinear analysis, and only a substitution process using different right-hand side vectors is required. Therefore, the computational cost of DSA is less than 10% that of the response analysis, which makes the design optimization process very efficient. Accuracy and efficiency of the proposed method is demonstrated by minimizing springback of the benchmark S-rail forming problem.

2. CAD-BASED GEOMETRIC MAPPING

In the stamping process, deformations of the tools (rigid punch, die, and blank holder) are generally ignorable. Therefore, in numerical analysis, these tools can be modeled as rigid bodies and their discretization is not needed. Only the blank sheet is modeled as the shell structure and discretized. A CAD geometric representation is utilized for both the tool surface and the shear deformable shell structure. Since the CAD surface representation used in this paper has C^1-continuity, its use for the tool surface provides a continuous contact force and surface normal vector, as well as a valid contact tangent stiffness matrix. The CAD representation of the tool surface alleviates significant amount of difficulty from a piecewise-linear contact surface in FEA. In addition, since no element information is generated in the meshfree method (which is used in this paper for numerical analysis), the surface information from the CAD model is necessary for constructing the surface normal vector and the mapping from the global to local coordinate.

2.1 Tool Surface Representation

In the CAD model, a surface geometry in a general three-dimensional space can be represented by using two parameters as [18]

$$\boldsymbol{x}^n(\xi,\eta) = \boldsymbol{U}(\xi)^T \boldsymbol{M}\boldsymbol{G}\boldsymbol{M}^T\boldsymbol{W}(\eta) \tag{1}$$

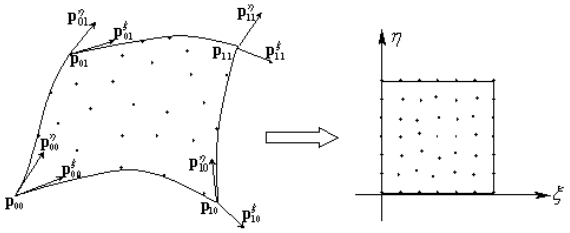

Figure 1. Parametric Representation of a Surface Geometry

where $\boldsymbol{U}(\xi)=[\xi^3,\xi^2,\xi,1]^T$ and $\boldsymbol{W}(\eta)=[\eta^3,\eta^2,\eta,1]^T$ are vectors in the parametric coordinates. In equation (1), $\boldsymbol{M}$ is a matrix defined as

$$\boldsymbol{M} = \begin{bmatrix} 2 & -2 & 1 & 1 \\ -3 & 3 & -2 & -1 \\ 0 & 0 & 1 & 0 \\ 1 & 0 & 0 & 0 \end{bmatrix} \tag{2}$$

and G is the surface geometric matrix defined as

$$\boldsymbol{G}=\begin{bmatrix} \boldsymbol{p}_{00} & \boldsymbol{p}_{01} & \boldsymbol{p}^{\eta}_{00} & \boldsymbol{p}^{\eta}_{01} \\ \boldsymbol{p}_{10} & \boldsymbol{p}_{11} & \boldsymbol{p}^{\eta}_{10} & \boldsymbol{p}^{\eta}_{11} \\ \boldsymbol{p}^{\xi}_{00} & \boldsymbol{p}^{\xi}_{01} & \boldsymbol{p}^{\xi\eta}_{00} & \boldsymbol{p}^{\xi\eta}_{01} \\ \boldsymbol{p}^{\xi}_{10} & \boldsymbol{p}^{\xi}_{11} & \boldsymbol{p}^{\xi\eta}_{10} & \boldsymbol{p}^{\xi\eta}_{11} \end{bmatrix}_{4\times4\times3} \tag{3}$$

where $\boldsymbol{p}_{ij}$ are coordinate of the corner points on the surface; $\boldsymbol{p}^{\xi}_{ij}$ and $\boldsymbol{p}^{\eta}_{ij}$ are tangent vectors in ξ and η directions; and $\boldsymbol{p}^{\xi\eta}_{ij}$ are twist vectors. Figure 1 shows the surface geometry and its transformation into the parametric coordinate.

2.2 Shell Structure

A general shell structure is represented by the neutral surface geometry and thickness data at each point. The neutral surface geometry can be represented using equation (1) and the thickness data is constructed using the information from the CAD surface representation. The surface representation method in equation (1) provides good flexibility from a computational viewpoint. For example, the normal vector on the surface at (ξ,η) can be obtained as

$$\boldsymbol{n}(\xi,\eta)=\frac{\boldsymbol{x}^{n}_{,\xi}\times\boldsymbol{x}^{n}_{,\eta}}{\left\|\boldsymbol{x}^{n}_{,\xi}\times\boldsymbol{x}^{n}_{,\eta}\right\|} \tag{4}$$

where, from equation (1),

$$\boldsymbol{x}^{n}_{,\xi}=\boldsymbol{U}(\xi)_{,\xi}^{T}\,\boldsymbol{M}\boldsymbol{G}\boldsymbol{M}^{T}\boldsymbol{W}(\eta) \tag{5}$$

$$\boldsymbol{x}^{n}_{,\eta}=\boldsymbol{U}(\xi)^{T}\,\boldsymbol{M}\boldsymbol{G}\boldsymbol{M}^{T}\boldsymbol{W}(\eta)_{,\eta} \tag{6}$$

The surface normal vector in equation (4) reduces a significant amount of discretization error that often occurs in the traditional FEA for frictional contact analysis.

For a shell structure with thickness $t(\xi,\eta)$, any points within the structure can be represented by

$$\boldsymbol{x}(\xi,\eta,\zeta)=\boldsymbol{U}(\xi)^{T}\,\boldsymbol{M}\boldsymbol{G}\boldsymbol{M}^{T}\boldsymbol{W}(\eta)+\zeta\frac{t}{2}\boldsymbol{n}(\xi,\eta) \tag{7}$$

where ζ=[−1,1] is the third parametric coordinate in the thickness direction. The Jacobian of the mapping can be obtained, from the relation in equation (7) as

$$\begin{aligned}\boldsymbol{x}_{,\xi}&=\boldsymbol{U}^{T}_{,\xi}\boldsymbol{M}\boldsymbol{G}\boldsymbol{M}^{T}\boldsymbol{W}+\zeta\frac{t}{2}\boldsymbol{n}_{,\xi}\\ \boldsymbol{x}_{,\eta}&=\boldsymbol{U}^{T}\boldsymbol{M}\boldsymbol{G}\boldsymbol{M}^{T}\boldsymbol{W}_{,\eta}+\zeta\frac{t}{2}\boldsymbol{n}_{,\eta}\\ \boldsymbol{x}_{,\zeta}&=\frac{t}{2}\boldsymbol{n}\end{aligned} \tag{8}$$

By defining x=[x_1, x_2, x_3] and ξ=[ξ_1, ξ_2, ξ_3]=[ξ, η, ζ] for notational convenience, the Jacobian of the mapping between the physical and the parametric coordinate can be represented by

$$\boldsymbol{J}_0=\frac{\partial x_i}{\partial\xi_j} \tag{9}$$

For the shell structure, the constitutive relation is given in the body-fixed, local coordinate system, whereas a displacement-strain relation is provided in the global coordinate system. The unit vectors in the local coordinate is calculated as

$$\boldsymbol{l}=\frac{\boldsymbol{x}^{n}_{,\xi}}{\left\|\boldsymbol{x}^{n}_{,\xi}\right\|},\quad \boldsymbol{n}=\frac{\boldsymbol{x}^{n}_{,\xi}\times\boldsymbol{x}^{n}_{,\eta}}{\left\|\boldsymbol{x}^{n}_{,\xi}\times\boldsymbol{x}^{n}_{,\eta}\right\|},\quad \boldsymbol{m}=\boldsymbol{n}\times\boldsymbol{l} \tag{10}$$

Using the relations in equation (10), the coordinate transformation can be obtained as

$$\boldsymbol{x}=\begin{bmatrix} l_1 & m_1 & n_1 \\ l_2 & m_2 & n_2 \\ l_3 & m_3 & n_3 \end{bmatrix}\boldsymbol{x}' \tag{11}$$

where $\boldsymbol{x}'$ is the coordinate of the corresponding point $\boldsymbol{x}$ in the local coordinate system.

3. CONTACT ANALYSIS

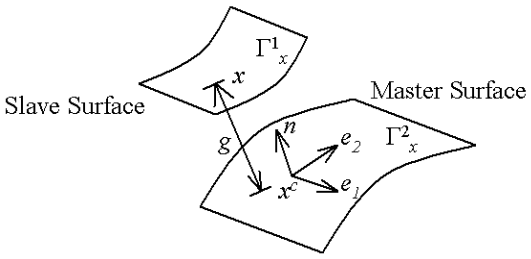

Figure 2. Contact Kinematics

In this section, contact analysis between a shell structure (a blank sheet) and tools (rigid punch, die, and blank holder) is described in continuum formulation. Figure 2 illustrates the contact kinematics between two surfaces, represented by Γ^1_x and Γ^2_x. Γ^1_x is designated as a slave surface, while Γ^2_x is designated as a master surface. In the stamping problem, the blank sheet is referred to as the slave body and the punch, die, and blank holder is referred to as the master body. Contact constraints are imposed such that the points on Γ^1_x cannot penetrate into Γ^2_x. The master surface is represented by the two parameters of the CAD geometric surface as $\boldsymbol{x}^c(\xi_1,\xi_2)$. Therefore, two tangential vectors and a normal vector on the master surface are defined as

$$\boldsymbol{e}_1=\boldsymbol{x}^{c}_{,1},\quad \boldsymbol{e}_2=\boldsymbol{x}^{c}_{,2},\quad \boldsymbol{n}=\boldsymbol{e}_1\times\boldsymbol{e}_2\big/\left\|\boldsymbol{e}_1\times\boldsymbol{e}_2\right\| \tag{12}$$

where $\boldsymbol{x}_{,\alpha}=\partial\boldsymbol{x}/\partial\xi_\alpha$, α=1,2. Note that $\boldsymbol{e}_1$ and $\boldsymbol{e}_2$ are not necessarily orthogonal to each other, but are tangent to the contact surface.

One of the most important steps in the contact analysis is to locate the contact point in accurate and efficient way. The contact point $\boldsymbol{x}^c\in\Gamma^2_x$ corresponding to the slave point $\boldsymbol{x}\in\Gamma^1_x$ is determined from the consistency condition,

$$\boldsymbol{e}_\alpha\cdot\left(\boldsymbol{x}-\boldsymbol{x}^c\right)=0,\quad \alpha=1,2 \tag{13}$$

Note that $\boldsymbol{x}^c$ is the closest projection point corresponding to $\boldsymbol{x}$. Using the normal gap function, which is the normal distance between two bodies, the impenetrability condition can be imposed as

$$g = \boldsymbol{n} \cdot \left(\boldsymbol{x} - \boldsymbol{x}^c \right) \geq 0 \tag{14}$$

It is known that the contact variational inequality is equivalent to the constrained minimization problem, which can be approximated using the Lagrange multiplier or penalty method. In this paper, the penalty method is used without introducing additional unknowns in the variational governing equation.

If a region denoted $\Gamma^c (\subset \Gamma_x^1)$ exists that violates the impenetrability condition of equation (14), then this region is penalized using a penalty function, which is defined as

$$P = \frac{1}{2} \omega_n \int_{\Gamma^c} g^2 d\Gamma \tag{15}$$

where ω_n is the penalty parameter. Let the symbol "over-bar" denote a variation of the quantity such that $\overline{\boldsymbol{z}}$ represents the displacement variation. The variation of the penalty function in equation (15) contains the variation of the gap function, which can be obtained from its definition as

$$\overline{g} = \boldsymbol{n} \cdot \left(\overline{\boldsymbol{z}} - \overline{\boldsymbol{z}}^c \right) \equiv \boldsymbol{n} \cdot \hat{\overline{\boldsymbol{z}}} \tag{16}$$

where the notations $\hat{\boldsymbol{z}} = \boldsymbol{z} - \boldsymbol{z}^c$ and $\hat{\overline{\boldsymbol{z}}} = \overline{\boldsymbol{z}} - \overline{\boldsymbol{z}}^c$ are used for the relative displacement and its variation between two contact points. Note that the variation of the normal vector $\boldsymbol{n}$ vanishes because it is orthogonal to the vector $(\boldsymbol{z} - \boldsymbol{z}^c)$.

The variation of the penalty function becomes the contact variational form, which is defined as

$$b_N \left({}^{n+1}\boldsymbol{z}, \overline{\boldsymbol{z}} \right) \equiv \overline{P} = \omega_n \int_{\Gamma^c} g \overline{g} d\Gamma \tag{17}$$

where $\omega_n g$ corresponds to the compressive normal force. The left superscript "n+1" denotes the configuration at time t_{n+1}.

By combining equation (17) with the structural energy form $a_\Omega \left({}^{n+1}\boldsymbol{z}, \overline{\boldsymbol{z}} \right)$ and load linear form $\ell_\Omega \left(\overline{\boldsymbol{z}} \right)$ presented by Choi *et al*. (equations (32) and (33), respectively, in [13]), the finite deformation elastoplastic nonlinear variational governing equation for the penalized contact condition becomes

$$a_\Omega \left({}^{n+1}\boldsymbol{z}, \overline{\boldsymbol{z}} \right) + b_N \left({}^{n+1}\boldsymbol{z}, \overline{\boldsymbol{z}} \right) = \ell_\Omega \left(\overline{\boldsymbol{z}} \right), \quad \forall \overline{\boldsymbol{z}} \in Z \tag{18}$$

Note that even if the structure encounters only elastic deformation, equation (18) is nonlinear since the inequality constraint is imposed throughout the penalty method. In equation (18),

$$Z = \left\{ \boldsymbol{z} \in \left[H^1 (\Omega) \right]^3 \middle| \boldsymbol{z}(\boldsymbol{x}) = 0, \quad \boldsymbol{x} \in \Gamma_g \right\} \tag{19}$$

is the space of kinematically admissible displacement, where $H^1(\Omega)$ is first-order Sobolev space and Γ_g is the essential boundary where the displacement is prescribed.

In this paper, the return-mapping algorithm on the subspace defined by the zero-normal stress condition is used for elastoplastic integration. In order to handle the finite deformation, the Hughes-Winget's incrementally objective integration schemes is used.

The nonlinear equation (18) can be solved using a Newton iterative method through linearization. The linearization of the structural energy form, $a_\Omega^* \left({}^{n+1}\boldsymbol{z}; \Delta\boldsymbol{z}, \overline{\boldsymbol{z}} \right)$, is given in Figure 3. The linearization of contact variational form, $b_N^* \left({}^{n+1}\boldsymbol{z}; \Delta\boldsymbol{z}, \overline{\boldsymbol{z}} \right)$, will be derived in next section for DSA. By combining the linearization of the contact variational form with that of the structural energy form, the incremental equation becomes

$$\begin{aligned} & a_\Omega^* \left({}^{n+1}\boldsymbol{z}^k; \Delta\boldsymbol{z}^{k+1}, \overline{\boldsymbol{z}} \right) + b_N^* \left({}^{n+1}\boldsymbol{z}^k; \Delta\boldsymbol{z}^{k+1}, \overline{\boldsymbol{z}} \right) \\ & \quad = \ell_\Omega \left(\overline{\boldsymbol{z}} \right) - a_\Omega \left({}^{n+1}\boldsymbol{z}^k, \overline{\boldsymbol{z}} \right) - b_N \left({}^{n+1}\boldsymbol{z}^k, \overline{\boldsymbol{z}} \right), \quad \forall \overline{\boldsymbol{z}} \in Z \end{aligned} \tag{20}$$

where the right superscript k denotes the current iteration counter. For a given load step, equation (20) is solved iteratively until the residual force vanishes. After convergence, the decomposed tangent stiffness matrix is stored to be used in DSA. The continuum-based DSA method for a finite deformation elastoplastic shell structure is developed by Choi *et al*. [13] and the result will be used here to combine with DSA for the frictional contact problem. Interested reader is referred to [13].

Structural Energy Form : $a_\Omega \left({}^{n+1}\boldsymbol{z}, \overline{\boldsymbol{z}} \right) = \int_\Omega \frac{\partial \overline{z}_i}{\partial\, {}^{n+1}x_j} \, {}^{n+1}\sigma_{ij} d\Omega$

Load Linear Form : $\ell_\Omega \left(\overline{\boldsymbol{z}} \right) = \int_\Omega \overline{z}_i f_i^b d\Omega + \int_\Omega \overline{z}_i f_i^s d\Gamma$

Linearized Structural Energy Form :

$$a_\Omega^* \left({}^{n+1}\boldsymbol{z}; \Delta\boldsymbol{z}, \overline{\boldsymbol{z}} \right) = \int_\Omega \frac{\partial \overline{z}_i}{\partial\, {}^{n+1}x_j} \left[C_{ijkl}^{\text{alg}} + \delta_{kl}\sigma_{ij} - \delta_{kj}\sigma_{il} \right] \frac{\partial \Delta z_k}{\partial\, {}^{n+1}x_l} d\Omega$$

Figure 3. Structural Energy and Load Linear Forms

4. DESIGN SENSITIVITY ANALYSIS OF CONTACT PROBLEM

For design of the stamping process, the design variables are the shape of the stamped workpiece (for multistage stamping process) and tool surfaces (punch, die, and blank holder). Even when the shape of the workpiece is initially flat and thus not design variable, the DSA formulation must include the design velocity field of the workpiece because the updated Lagrangian formulation is used for the nonlinear analysis. For DSA of the contact problem, instead of differentiating the contact variational inequality, the penalty-approximated variational equation is differentiated with respect to the design variable.

4.1 Material Derivative Formulas

In shape and configuration DSA, a material point ${}^0\boldsymbol{x}$ is moved to a new point ${}^0\boldsymbol{x}_\tau \left(= {}^0\boldsymbol{x} + \tau\, {}^0\boldsymbol{V} \right)$ due to design perturbation. A design velocity field ${}^0\boldsymbol{V}$ represents the direction of the design perturbation, and τ is a scalar parameter to control the perturbation size. In the updated Lagrangian formulation, the reference frame is updated after each incremental analysis using the following relation

$${}^n\boldsymbol{x} = {}^0\boldsymbol{x} + {}^n\boldsymbol{z} \tag{21}$$

where ${}^n\boldsymbol{x}$ is spatial coordinate at time t_n and ${}^n\boldsymbol{z}$ is the sum of the incremental displacement up to time t_n. By differentiating the above relation, the following design velocity update formula is obtained

$$\frac{d}{d\tau}\left({}^n\boldsymbol{x}_\tau\right)\Big|_{\tau=0} = \frac{d}{d\tau}\left({}^0\boldsymbol{x}_\tau + {}^n\boldsymbol{z}_\tau\right)\Big|_{\tau=0} = {}^0\boldsymbol{V} + {}^n\dot{\boldsymbol{z}} = {}^n\boldsymbol{V} \quad (22)$$

The superposed dot will be used to denote the material derivative of a function throughout this paper. Note that even when the shape of the slave surface (workpiece) is not a design variable, and thus initial design velocity field, ${}^0\boldsymbol{V}$, is zero, the design velocity field at time t_n is nonzero due to ${}^n\dot{\boldsymbol{z}}$. Using the relation in equation (22), the material derivative of the structural point on the slave surface at the current configuration becomes

$$\frac{d}{d\tau}\left({}^{n+1}\boldsymbol{x}_\tau\right)\Big|_{\tau=0} = \frac{d}{d\tau}\left({}^n\boldsymbol{x}_\tau + \Delta\boldsymbol{z}_\tau\right)\Big|_{\tau=0} = {}^n\boldsymbol{V} + \Delta\dot{\boldsymbol{z}} \quad (23)$$

On the other hand, the perturbation of the contact point on the master surface (tool surface) can be obtained by using the chain rule and by perturbing the natural coordinate corresponding to the contact point in the tangential direction as

$$\frac{d}{d\tau}\left({}^{n+1}\boldsymbol{x}_\tau^c\right)\Big|_{\tau=0} = {}^n\boldsymbol{V}^c + \Delta\dot{\boldsymbol{z}}^c + \boldsymbol{e}_\alpha\dot{\xi}_\alpha \quad (24)$$

where a summation rule is used for the repeated indices.

The material derivatives of the structural energy form is [13]

$$\frac{d}{d\tau}\left[a_\Omega\left({}^{n+1}\boldsymbol{z}_\tau, \bar{\boldsymbol{z}}_\tau\right)\right]\Big|_{\tau=0} = a_\Omega^*\left({}^{n+1}\boldsymbol{z}; \Delta\dot{\boldsymbol{z}}, \bar{\boldsymbol{z}}\right) + a_V'\left({}^{n+1}\boldsymbol{z}, \bar{\boldsymbol{z}}\right) \quad (25)$$

where $a_\Omega^*\left({}^{n+1}\boldsymbol{z}; \Delta\dot{\boldsymbol{z}}, \bar{\boldsymbol{z}}\right)$ is the same form as the linearized energy form in equation (20) by substituting $\Delta\boldsymbol{z}^k$ for $\Delta\dot{\boldsymbol{z}}$. $a_V'\left({}^{n+1}\boldsymbol{z}, \bar{\boldsymbol{z}}\right)$ is the structural fictitious load form, which includes all known terms from the response analysis and DSA up to the previous time step and its expression is given in Figure 4. The material derivative of the load linear form is

$$\frac{d}{d\tau}\left[\ell_\Omega\left(\bar{\boldsymbol{z}}_\tau\right)\right]\Big|_{\tau=0} = \ell_V'\left(\bar{\boldsymbol{z}}\right) \quad (26)$$

Structural Fictitious Load Form :

$$a_V'\left({}^{n+1}\boldsymbol{z}, \bar{\boldsymbol{z}}\right) = \int_\Omega \left[\varepsilon_{ij}^V\left(\bar{\boldsymbol{z}}\right)\sigma_{ij} + \frac{\partial \bar{z}_i}{\partial\, {}^{n+1}x_j} C_{ijkl}^{\text{alg}} + \frac{\partial \bar{z}_i}{\partial\, {}^{n+1}x_j}\sigma_{ij}^{fic} + \frac{\partial \bar{z}_i}{\partial\, {}^{n+1}x_j}\sigma_{ij} div\, {}^n\boldsymbol{V}\right] d\Omega$$

Figure 4. Fictitious Load Form for DSA

4.2 Design Velocity Field Computation

The computation of ${}^0\boldsymbol{V}$ and ${}^0\boldsymbol{V}^c$ are directly related to the parametric representation of the surface as given in equation (1). For example, Figure 5 shows die geometry, which is composed of three surfaces. Each surface is characterized by its surface geometric matrix $\boldsymbol{G}_{i=1,2,3}$ as in equation (3). If the corner radius R is considered as a design parameter, the design dependence of the surface is written as

$${}^0\boldsymbol{x}_i^c(R) = \boldsymbol{U}(\xi)^T\, \boldsymbol{M}\boldsymbol{G}_i(R)\boldsymbol{M}^T\boldsymbol{W}(\eta) \qquad i = 1,2,3 \quad (27)$$

Since geometric matrix $\boldsymbol{G}_i(R)$ is a function of the corner radius R, the design velocity can be obtained by perturbing R to $R + \tau\delta R$, and the differentiating with respect to τ as

$$\begin{aligned} {}^0\boldsymbol{V}_i^c &= \frac{d\, {}^0\boldsymbol{x}_i^c\left(R + \tau\delta R\right)}{d\tau}\Big|_{\tau=0} \\ &= \boldsymbol{U}(\xi)^T\, \boldsymbol{M}\left(\frac{\partial \boldsymbol{G}_i}{\partial R}\delta R\right)\boldsymbol{M}^T\boldsymbol{W}(\eta) \\ &= \boldsymbol{U}(\xi)^T\, \boldsymbol{M}\left(\boldsymbol{G}_i^{new} - \boldsymbol{G}_i\right)\boldsymbol{M}^T\boldsymbol{W}(\eta) \end{aligned} \quad (28)$$

where $\boldsymbol{G}_i^{new}$ is a geometric matrix of each surface when the corner radius is changed to R_{new} using the CAD model.

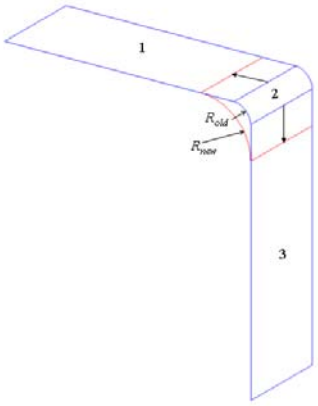

Figure 5. Example of Die Composed of Three Surfaces

Suppose the contact surface Γ^c change its shape due to design perturbation. The contact form in equation (17) depends on the design in two ways: explicitly through the contact surface design change and implicitly through the response $\boldsymbol{z}$. The material derivative of the contact form can be obtained as

$$\frac{d}{d\tau}\left[b_N\left({}^{n+1}\boldsymbol{z}, \bar{\boldsymbol{z}}\right)\right]\Big|_{\tau=0} = \omega_n \int_{\Gamma^c}\left[\dot{g}\bar{g} + g\dot{\bar{g}} + gg\kappa\, {}^nV_n\right] d\Gamma \quad (29)$$

where κ is the curvature of the master surface, and ${}^n\boldsymbol{V}$ is the normal component of the design velocity. For DSA, $\dot{g}$ and $\dot{\bar{g}}$ need to be expressed in terms of the implicit term $\Delta\dot{\boldsymbol{z}}$ and the explicit term ${}^n\boldsymbol{V}$. From its definition in equation (14), the material derivative of the gap function can be obtained as

$$\dot{g} = \boldsymbol{n}\cdot\left(\Delta\dot{\boldsymbol{z}} + {}^n\hat{\boldsymbol{V}}\right) \quad (30)$$

where ${}^n\hat{\boldsymbol{V}} \equiv {}^n\boldsymbol{V} - {}^n\boldsymbol{V}^c$. However, the derivation of $\dot{\bar{g}}$ is not straightforward and the relation of $\bar{\boldsymbol{z}} = \bar{g}\boldsymbol{n} + g\bar{\boldsymbol{n}} + \boldsymbol{e}_\alpha\bar{\xi}_\alpha$ is needed to make the stiffness matrix symmetric. Equation (30) thus becomes

$$\dot{\bar{g}} = -\boldsymbol{n}\cdot\bar{\boldsymbol{z}}^c_{,\alpha}\dot{\xi}_\alpha - \left(\boldsymbol{n}\cdot\dot{\boldsymbol{e}}_\alpha\right)\bar{\xi}_\alpha + g\left(\boldsymbol{n}\cdot\dot{\boldsymbol{e}}_\alpha\right)m^{-1}_{\alpha\beta}\left(\boldsymbol{n}\cdot\bar{\boldsymbol{e}}_\beta\right) \quad (31)$$

where $m_{\alpha\beta} = \boldsymbol{e}_\alpha\cdot\boldsymbol{e}_\beta$. In equation (31),

$$\dot{\boldsymbol{e}}_\alpha \equiv \frac{d}{d\tau}\left({}^{n+1}\boldsymbol{x}^c_{,\alpha}\right)\Big|_{\tau=0} = \Delta\dot{\boldsymbol{z}}^c_{,\alpha} + {}^n\boldsymbol{V}^c_{,\alpha} + {}^{n+1}\boldsymbol{x}^c_{,\alpha\beta}\dot{\xi}_\beta \quad (32)$$

The expression of $\dot{\xi}_\beta$ can be obtained from the consistency condition in equation (13) as

$$\begin{aligned}\dot{\xi}_\beta &= A^{-1}_{\alpha\beta}\left(\Delta\dot{\boldsymbol{z}}\cdot\boldsymbol{e}_\alpha\right) + A^{-1}_{\alpha\beta}\left({}^n\hat{\boldsymbol{V}}\cdot\boldsymbol{e}_\alpha + g\boldsymbol{n}\cdot{}^n\boldsymbol{V}^c_{,\alpha}\right)\\ &\equiv \xi_\beta\left(\Delta\dot{\boldsymbol{z}}\right) + \xi_\beta\left({}^n\boldsymbol{V}\right)\end{aligned} \quad (33)$$

where $A_{\alpha\beta} = m_{\alpha\beta} - g\boldsymbol{n}\cdot{}^{n+1}\boldsymbol{x}^c_{,\alpha\beta}$. By using the relations from equations (30) to (33), the material derivative of the contact variational form can be separated into two parts: the implicitly dependent and the explicitly dependent parts, as

$$\frac{d}{d\tau}\left[b_N\left({}^{n+1}\boldsymbol{z}_\tau, \bar{\boldsymbol{z}}_\tau\right)\right]\Big|_{\tau=0} = b^*_N\left({}^{n+1}\boldsymbol{z}; \Delta\dot{\boldsymbol{z}}, \bar{\boldsymbol{z}}\right) + b'_N\left({}^{n+1}\boldsymbol{z}, \bar{\boldsymbol{z}}\right) \quad (34)$$

where

$$\begin{aligned}b^*_N\left({}^{n+1}\boldsymbol{z}; \Delta\dot{\boldsymbol{z}}, \bar{\boldsymbol{z}}\right) &= \omega_n\int_{\Gamma_c}\hat{\bar{\boldsymbol{z}}}\cdot\boldsymbol{n}\boldsymbol{n}\cdot\Delta\hat{\dot{\boldsymbol{z}}}d\Gamma\\ &-\omega_n\int_{\Gamma_c} g\left[\boldsymbol{n}\cdot\bar{\boldsymbol{z}}^c_{,\alpha}\xi_\alpha\left(\Delta\dot{\boldsymbol{z}}\right) + \boldsymbol{n}\cdot\Delta\dot{\boldsymbol{z}}^c_{,\alpha}\bar{\xi}_\alpha\right.\\ &\left.+\boldsymbol{n}\cdot{}^{n+1}\boldsymbol{x}^c_{,\alpha\beta}\bar{\xi}_\alpha\xi\left(\Delta\dot{\boldsymbol{z}}\right)\right]d\Gamma\\ &+\omega_n\int_{\Gamma_c} g^2\left[\left(n\cdot e_\alpha\left(\Delta\dot{\boldsymbol{z}}\right)\right)m^{-1}_{\alpha\beta}\left(\boldsymbol{n}\cdot\bar{\boldsymbol{e}}_\beta\right)\right]d\Gamma\end{aligned} \quad (35)$$

is the same form as the linearization of the contact variational form in equation (17) if we substitute $\Delta\boldsymbol{z}^k$ for $\Delta\dot{\boldsymbol{z}}$. This linearized bilinear form is used in the incremental equation (20) of the governing variational equation (18). The second term on the right of equation (34) is the fictitious load form due to frictionless contact, which is defined as

$$b'_N\left({}^{n+1}\boldsymbol{z}, \bar{\boldsymbol{z}}\right) \equiv b^*_N\left({}^{n+1}\boldsymbol{z}; {}^n\boldsymbol{V}, \bar{\boldsymbol{z}}\right) + \omega_n\int_{\Gamma_c}\left[\kappa g\bar{\boldsymbol{z}}\cdot\boldsymbol{n}\,{}^n\boldsymbol{V}_n\right]d\Gamma \quad (36)$$

5. FRICTIONAL CONTACT DESIGN SENSITIVITY ANALYSIS

When friction exists on the contact surface, the structure experiences a tangential frictional force, in addition to the normal contact force. Since the frictional behavior is complicated, many idealizations have been made. The Coulomb friction law is one of the frequently used methods to describe frictional behavior. However, this method presents numerical difficulties because of a discontinuity of the frictional force. A more advanced friction model assumes that the frictional force elastically increases until it reaches the limit value, and then the macroscopic slip occurs along the contact surface. This model is based on the experimental observation and corresponds to the non-associative flow rule in elastoplasticity. Thus, the return-mapping algorithm can be used to determine the frictional force like in elastoplasticity.

5.1 Frictional Model

The frictional force appears parallel to the contact surface and is expressed as

$$\boldsymbol{f} = f_\alpha\boldsymbol{e}^\alpha \quad (37)$$

where $\boldsymbol{e}^\alpha$ is the dual basis of $\boldsymbol{e}_\alpha$ and has the following relation:

$$\begin{aligned}\boldsymbol{e}^\alpha\cdot\boldsymbol{e}_\beta &= \delta_{\alpha\beta}\\ \boldsymbol{e}^\alpha &= \mathrm{m}^{-1}_{\alpha\beta}\boldsymbol{e}_\beta\end{aligned} \quad (38)$$

where $m_{\alpha\beta} = \boldsymbol{e}_\alpha\cdot\boldsymbol{e}_\beta$ and $\delta_{\alpha\beta}$ is the Kronecker delta symbol, i.e., having a value of one when $\alpha = \beta$, and otherwise remaining at zero. The frictional contact form of the problem can then be defined by multiplying the frictional force by the virtual relative slip as

$$b_T\left(\boldsymbol{z}, \bar{\boldsymbol{z}}\right) = \int_{\Gamma^c} f_\alpha\bar{\xi}_\alpha d\Gamma \quad (39)$$

The expression $\bar{\xi}_\alpha$ can be obtained from the consistency condition in equation (13) as

$$\bar{\xi}_\beta = A^{-1}_{\alpha\beta}\left(\hat{\bar{\boldsymbol{z}}}\cdot\boldsymbol{e}_\alpha + g\boldsymbol{n}\cdot\bar{\boldsymbol{z}}^c_{,\alpha}\right) \quad (40)$$

In the regularized frictional model, frictional force f_α is calculated by using a return-mapping algorithm like in elastoplasticity. Initially, the frictional force increases in proportion to the relative slip amount. This trial frictional force is then compared with the limit value $\mu\omega_N g$, where μ is Coulomb friction coefficient. If the trial force is smaller than the limit value, then the trial force becomes the frictional force (stick condition). If the trial force is greater than the limit value, then the limit value is used for the frictional force (slip condition). Figure 6 shows the frictional force used in this paper.

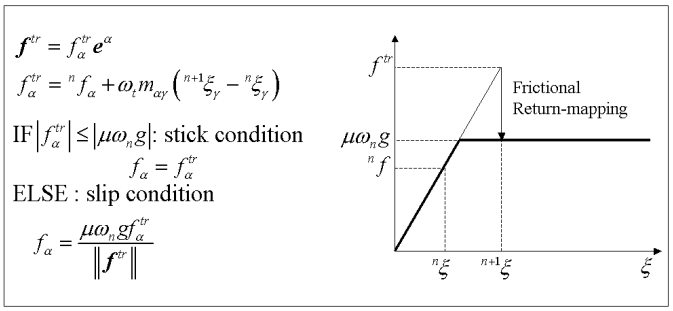

Figure 6. Return-mapping Algorithm for Frictional Force

As with the frictionless contact form, the nonlinear frictional contact form in equation (39) has to be linearized as part of the implicit solution process. The linearized frictional contact form is denoted by $b^*_T\left(\boldsymbol{z}; \Delta\boldsymbol{z}, \bar{\boldsymbol{z}}\right)$, an expression that is developed in the following section. If the following notations are used,

$$\begin{aligned}b_\Gamma\left({}^{n+1}\boldsymbol{z}, \bar{\boldsymbol{z}}\right) &= b_N\left({}^{n+1}\boldsymbol{z}, \bar{\boldsymbol{z}}\right) + b_T\left({}^{n+1}\boldsymbol{z}, \bar{\boldsymbol{z}}\right)\\ b^*_\Gamma\left({}^{n+1}\boldsymbol{z}; \Delta\boldsymbol{z}, \bar{\boldsymbol{z}}\right) &= b^*_N\left({}^{n+1}\boldsymbol{z}; \Delta\boldsymbol{z}, \bar{\boldsymbol{z}}\right) + b^*_T\left({}^{n+1}\boldsymbol{z}; \Delta\boldsymbol{z}, \bar{\boldsymbol{z}}\right)\end{aligned} \quad (41)$$

then linearized incremental equation can be extended to the frictional contact problem as

$$a_{\Omega}^{*}\left({}^{n+1}\mathbf{z}^{k};\Delta\mathbf{z}^{k+1},\overline{\mathbf{z}}\right)+b_{\Gamma}^{*}\left({}^{n+1}\mathbf{z}^{k};\Delta\mathbf{z}^{k+1},\overline{\mathbf{z}}\right)$$
$$=\ell_{\Omega}\left(\overline{\mathbf{z}}\right)-a_{\Omega}\left({}^{n+1}\mathbf{z}^{k},\overline{\mathbf{z}}\right)-b_{\Gamma}\left({}^{n+1}\mathbf{z}^{k},\overline{\mathbf{z}}\right),\quad\forall\overline{\mathbf{z}}\in Z \tag{42}$$

It is shown in the next section that the same left side of equation (42) can be used in DSA.

5.2 Design Sensitivity Formulation of Friction Form

Unlike the frictionless contact form, the frictional contact form depends on analysis results at the previous load step because of the updating algorithm of the frictional force. Thus, the sensitivity equation constitutes three parts: implicitly dependent terms, explicitly dependent terms, and path-dependent terms. The material derivative of the frictional contact form can be obtained from equation (39) as

$$\frac{d}{d\tau}\left[b_{T}\left({}^{n+1}\mathbf{z},\overline{\mathbf{z}}\right)\right]\Big|_{\tau=0}=\int_{\Gamma^{c}}\left(\dot{f}_{\alpha}\overline{\xi}_{\alpha}+f_{\alpha}\dot{\overline{\xi}}_{\alpha}+\kappa f_{\alpha}\overline{\xi}_{\alpha}\,{}^{n}V\right)d\Gamma \tag{43}$$

The material derivative of $\overline{\xi}_{\beta}$ can be obtained from equation (40) as

$$\begin{aligned}A_{\alpha\beta}\dot{\overline{\xi}}_{\beta}=&-\mathbf{e}_{\alpha}\cdot\overline{\mathbf{z}}_{,\gamma}^{c}\dot{\xi}_{\gamma}+\hat{\overline{\mathbf{z}}}\cdot\dot{\mathbf{e}}_{\alpha}+\overline{\mathbf{e}}_{\alpha}\cdot\Delta\hat{\dot{\mathbf{z}}}-\overline{\mathbf{e}}_{\alpha}\cdot\mathbf{e}_{\beta}\dot{\xi}_{\beta}\\&-\dot{\mathbf{e}}_{\alpha}\cdot\mathbf{e}_{\beta}\overline{\xi}_{\beta}-\left[\mathbf{e}_{\alpha}\cdot\mathbf{x}_{,\gamma\beta}^{c}-g\mathbf{n}\cdot\mathbf{x}_{,\alpha\gamma\beta}^{c}\right]\dot{\xi}_{\beta}\overline{\xi}_{\gamma}\\&-\mathbf{e}_{\alpha}\cdot\Delta\dot{\mathbf{z}}_{,\beta}^{c}\overline{\xi}_{\gamma}+g\mathbf{n}\cdot\Delta\dot{\mathbf{z}}_{,\alpha\gamma}^{c}\overline{\xi}_{\gamma}+g\mathbf{n}\cdot\overline{\mathbf{z}}_{,\alpha\beta}^{c}\dot{\xi}_{\beta}\\&+\overline{\mathbf{e}}_{\alpha}\cdot{}^{n}\hat{\mathbf{V}}-\mathbf{e}_{\alpha}\cdot{}^{n}\mathbf{V}_{,\beta}^{c}\overline{\xi}_{\gamma}+g\mathbf{n}\cdot{}^{n}\mathbf{V}_{,\alpha\gamma}^{c}\overline{\xi}_{\gamma}\end{aligned} \tag{44}$$

Note that equation (44) includes the implicitly dependent $\left(\Delta\dot{\mathbf{z}}\right)$ and the explicitly dependent term $\left({}^{n}\mathbf{V}\right)$. No path-dependent term exists, and the expression is the same for both stick and slip conditions.

For the stick condition, the traction force increases in proportion to the amount of relative slip between two contact surfaces. The material derivative of the frictional force in equation (37) becomes

$$\begin{aligned}{}^{n+1}\dot{f}_{\alpha}=&\omega_{t}\Phi_{\alpha\beta}\xi_{\beta}\left(\Delta\dot{\mathbf{z}}\right)\\&+\omega_{t}\left[\mathbf{e}_{\beta}\cdot\Delta\dot{\mathbf{z}}_{,\alpha}^{c}+\mathbf{e}_{\alpha}\cdot\Delta\dot{\mathbf{z}}_{,\beta}^{c}\right]\left({}^{n+1}\xi_{\beta}-{}^{n}\xi_{\beta}\right)\\&+\omega_{t}\Phi_{\alpha\beta}\xi_{\beta}\left({}^{n}\mathbf{V}\right)\\&+\omega_{t}\left[\mathbf{e}_{\beta}\cdot{}^{n}\mathbf{V}_{,\alpha}^{c}+\mathbf{e}_{\alpha}\cdot{}^{n}\mathbf{V}_{,\beta}^{c}\right]\left({}^{n+1}\xi_{\beta}-{}^{n}\xi_{\beta}\right)\\&+{}^{n}\dot{f}_{\alpha}+\omega_{t}m_{\alpha\beta}\,{}^{n}\dot{\xi}_{\beta}\end{aligned} \tag{45}$$

where $\Phi_{\alpha\beta}\equiv\omega_{t}\left\{\left[\mathbf{x}_{,\alpha\beta}^{c}\cdot\mathbf{e}_{\gamma}+\mathbf{e}_{\alpha}\cdot\mathbf{x}_{,\gamma\beta}^{c}\right]\left({}^{n+1}\xi_{\gamma}-{}^{n}\xi_{\gamma}\right)+m_{\alpha\beta}\right\}$. In equation (45), first and second lines represent the implicitly dependent term, third and fourth lines represent the explicitly dependent term, and firth line represents the path-dependent term.

By substituting equations (44) and (45) into equation (43), the material derivative of the frictional contact form is explicitly obtained in terms of $\Delta\dot{\mathbf{z}}$, ${}^{n}\mathbf{V}$, and the path-dependent terms, as

$$\frac{d}{d\tau}\left[b_{T}\left({}^{n+1}\mathbf{z},\overline{\mathbf{z}}\right)\right]\Big|_{\tau=0}\equiv b_{T}^{*}\left({}^{n+1}\mathbf{z};\Delta\dot{\mathbf{z}},\overline{\mathbf{z}}\right)+b_{T}'\left({}^{n+1}\mathbf{z},\overline{\mathbf{z}}\right) \tag{46}$$

where the linearized friction form is defined by collecting all terms that include $\Delta\dot{\mathbf{z}}$ as

$$\begin{aligned}b_{T}^{*}\left({}^{n+1}\mathbf{z};\Delta\dot{\mathbf{z}},\overline{\mathbf{z}}\right)=\int_{\Gamma^{c}}\Big\{&\omega_{t}\Phi_{\alpha\beta}\xi_{\beta}\left(\Delta\dot{\mathbf{z}}\right)\overline{\xi}_{\alpha}\\&+\omega_{t}\left[\Delta\dot{\mathbf{z}}_{,\alpha}^{c}\cdot\mathbf{e}_{\beta}+\mathbf{e}_{\alpha}\cdot\Delta\dot{\mathbf{z}}_{,\beta}^{c}\right]\left({}^{n+1}\xi_{\beta}-{}^{n}\xi_{\beta}\right)\overline{\xi}_{\alpha}\\&+f_{\alpha}A_{\alpha\beta}^{-1}\Big(-\mathbf{e}_{\alpha}\cdot\overline{\mathbf{z}}_{,\gamma}^{c}\xi_{\gamma}\left(\Delta\dot{\mathbf{z}}\right)+\hat{\overline{\mathbf{z}}}\cdot\mathbf{e}_{\alpha}\left(\Delta\dot{\mathbf{z}}\right)\\&+\overline{\mathbf{e}}_{\alpha}\cdot\Delta\hat{\dot{\mathbf{z}}}-\overline{\mathbf{e}}_{\alpha}\cdot\mathbf{e}_{\beta}\xi_{\beta}\left(\Delta\dot{\mathbf{z}}\right)\\&+\mathbf{e}_{\alpha}\left(\Delta\dot{\mathbf{z}}\right)\cdot\mathbf{e}_{\beta}\overline{\xi}_{\beta}+g\mathbf{n}\cdot\overline{\mathbf{z}}_{,\alpha\beta}^{c}\xi_{\beta}\left(\Delta\dot{\mathbf{z}}\right)\\&-\left[\mathbf{e}_{\alpha}\cdot\mathbf{x}_{,\gamma\beta}^{c}-g\mathbf{n}\cdot\mathbf{x}_{,\alpha\gamma\beta}^{c}\right]\xi_{\beta}\left(\Delta\dot{\mathbf{z}}\right)\overline{\xi}_{\gamma}\\&-\mathbf{e}_{\alpha}\cdot\Delta\dot{\mathbf{z}}_{,\beta}^{c}\overline{\xi}_{\gamma}+g\mathbf{n}\cdot\Delta\dot{\mathbf{z}}_{,\alpha\gamma}^{c}\overline{\xi}_{\gamma}\Big)\Big\}d\Gamma\end{aligned} \tag{47}$$

and the fictitious load form due to friction is obtained by collecting those explicitly dependent terms and path-dependent terms as

$$\begin{aligned}b_{T}'\left({}^{n+1}\mathbf{z},\overline{\mathbf{z}}\right)=&b_{T}^{*}\left({}^{n+1}\mathbf{z};{}^{n}\mathbf{V},\overline{\mathbf{z}}\right)+\int_{\Gamma^{c}}\kappa f_{\alpha}\overline{\xi}_{\alpha}\,{}^{n}\mathbf{V}d\Gamma\\&+\int_{\Gamma^{c}}\left({}^{n}\dot{f}_{\alpha}\overline{\xi}_{\alpha}+\omega_{t}m_{\alpha\beta}\overline{\xi}_{\alpha}\,{}^{n}\dot{\xi}_{\beta}\right)d\Gamma\end{aligned} \tag{48}$$

For the slip condition, the magnitude of the frictional force is determined from the normal contact force, while the applied direction is parallel to the trial force. From the return-mapping algorithm given in Figure 6, the material derivative of the frictional force for the slip condition is obtained as

$$\begin{aligned}{}^{n+1}\dot{f}_{\alpha}=&\mu\omega_{n}p_{\alpha}\mathbf{n}\cdot\left(\Delta\dot{\mathbf{z}}+{}^{n}\hat{\mathbf{V}}\right)\\&+\frac{\mu\omega_{n}g}{\left\|\mathbf{f}^{tr}\right\|}\left[\dot{f}_{\alpha}^{tr}-p_{\alpha}p^{\beta}\dot{f}_{\beta}^{tr}-f_{\alpha}^{tr}p_{\beta}\mathbf{p}\cdot\dot{\mathbf{e}}^{\beta}\right]\end{aligned} \tag{49}$$

where $\mathbf{p}=\mathbf{f}^{tr}/\left\|\mathbf{f}^{tr}\right\|$, $p_{\alpha}=f_{\alpha}^{tr}/\left\|\mathbf{f}^{tr}\right\|$, and $p^{\beta}=\mathbf{p}\cdot\mathbf{e}^{\beta}$. In equation (49), $\dot{f}_{\alpha}^{tr}$ is the same as in equation (45) for the stick condition. By substituting equations (44) and (49) into equation (43), the material derivative of the frictional contact form is obtained. If the implicitly dependent terms are combined, the linearized frictional contact form can be obtained as

$$\begin{aligned}b_{T}^{*}\left({}^{n+1}\mathbf{z};\Delta\dot{\mathbf{z}},\overline{\mathbf{z}}\right)=&\mu\omega_{n}\int_{\Gamma^{c}}\Big\{p_{\alpha}\overline{\xi}_{\alpha}\mathbf{n}\cdot\Delta\dot{\mathbf{z}}\\&+\omega_{t}g\left(\delta_{\alpha\beta}-p_{\alpha}p^{\beta}\right)/\left\|\mathbf{f}^{tr}\right\|\Big[\Phi_{\beta\gamma}\xi_{\gamma}\left(\Delta\dot{\mathbf{z}}\right)\\&+\omega_{t}\left[\mathbf{e}_{\beta}\cdot\Delta\dot{\mathbf{z}}_{,\gamma}^{c}+\Delta\dot{\mathbf{z}}_{,\beta}^{c}\cdot\mathbf{e}_{\gamma}\right]\left({}^{n+1}\xi_{\gamma}-{}^{n}\xi_{\gamma}\right)\Big]\overline{\xi}_{\alpha}\Big\}d\Gamma\\&-\mu\omega_{n}\int_{\Gamma^{c}}\Big\{gp_{\alpha}p^{\beta}\overline{\xi}_{\alpha}\Big\{\Big[\mathbf{p}\cdot\mathbf{x}_{,\beta\gamma}^{c}\\&-\left(\left[\mathbf{x}_{,\beta\gamma}^{c}\cdot\mathbf{e}_{\phi}+\mathbf{e}_{\beta}\cdot\mathbf{x}_{,\phi\gamma}^{c}\right]\mathbf{p}\cdot\mathbf{e}^{\phi}\right)\Big]\xi_{\gamma}\left(\Delta\dot{\mathbf{z}}\right)\\&\mathbf{p}\cdot\Delta\dot{\mathbf{z}}_{,\beta}^{c}-\left(\Delta\dot{\mathbf{z}}_{,\beta}^{c}\cdot\mathbf{e}_{\gamma}+\Delta\dot{\mathbf{z}}_{,\gamma}^{c}\cdot\mathbf{e}_{\beta}\right)\mathbf{p}\cdot\mathbf{e}^{\gamma}\Big\}\Big\}d\Gamma\\&\int_{\Gamma^{c}}\Big\{f_{\alpha}A_{\alpha\beta}^{-1}\Big(-\mathbf{e}_{\alpha}\cdot\overline{\mathbf{z}}_{,\gamma}^{c}\xi_{\gamma}\left(\Delta\dot{\mathbf{z}}\right)+\hat{\overline{\mathbf{z}}}\cdot\mathbf{e}_{\alpha}\left(\Delta\dot{\mathbf{z}}\right)\\&+\overline{\mathbf{e}}_{\alpha}\cdot\Delta\hat{\dot{\mathbf{z}}}-\overline{\mathbf{e}}_{\alpha}\cdot\mathbf{e}_{\beta}\xi_{\beta}\left(\Delta\dot{\mathbf{z}}\right)+\mathbf{e}_{\alpha}\left(\Delta\dot{\mathbf{z}}\right)\cdot\mathbf{e}_{\beta}\overline{\xi}_{\beta}\\&+g\mathbf{n}\cdot\overline{\mathbf{z}}_{,\alpha\beta}^{c}\xi_{\beta}\left(\Delta\dot{\mathbf{z}}\right)--\mathbf{e}_{\alpha}\cdot\Delta\dot{\mathbf{z}}_{,\beta}^{c}\overline{\xi}_{\gamma}+g\mathbf{n}\cdot\Delta\dot{\mathbf{z}}_{,\alpha\gamma}^{c}\overline{\xi}_{\gamma}\\&-\left[\mathbf{e}_{\alpha}\cdot\mathbf{x}_{,\gamma\beta}^{c}-g\mathbf{n}\cdot\mathbf{x}_{,\alpha\gamma\beta}^{c}\right]\xi_{\beta}\left(\Delta\dot{\mathbf{z}}\right)\overline{\xi}_{\gamma}\Big)\Big\}d\Gamma\end{aligned} \tag{50}$$

In a similar way, the explicitly dependent terms and path-dependent terms are combined to define the fictitious load form due to friction as

$$b'_T\left({}^{n+1}\mathbf{z},\bar{\mathbf{z}}\right)=b^*_T\left({}^{n+1}\mathbf{z}^k;{}^n\mathbf{V},\bar{\mathbf{z}}\right)+\int_{\Gamma^c}\kappa f_\alpha\bar{\xi}_\alpha\,{}^n\mathbf{V}d\Gamma$$
$$\int_{\Gamma^c}\frac{\mu\omega_n g}{\left\|\mathbf{f}^{tr}\right\|}\left(\delta_{\alpha\beta}-p_\alpha p^\beta\right)\left({}^n\dot{f}_\alpha+\omega_t m_{\alpha\beta}\,{}^n\dot{\xi}_\beta\right)\bar{\xi}_\alpha d\Gamma \quad (51)$$

By adding equations (36) and (48) for the stick condition, or equations (36) and (51) for the slip condition, the total fictitious load from due to frictional contact can be defined as

$$b'_V\left({}^{n+1}\mathbf{z},\bar{\mathbf{z}}\right)\equiv b'_N\left({}^{n+1}\mathbf{z},\bar{\mathbf{z}}\right)+b'_T\left({}^{n+1}\mathbf{z},\bar{\mathbf{z}}\right) \quad (52)$$

Finally, by adding the material derivatives in equations (25), (34), and (46), and using equation (52), the design sensitivity equation for the frictional contact problem is obtained as

$$a^*_\Omega\left({}^{n+1}\mathbf{z};\Delta\dot{\mathbf{z}},\bar{\mathbf{z}}\right)+b^*_\Gamma\left({}^{n+1}\mathbf{z};\Delta\dot{\mathbf{z}},\bar{\mathbf{z}}\right)=\ell'_V\left(\bar{\mathbf{z}}\right)$$
$$-a'_V\left({}^{n+1}\mathbf{z},\bar{\mathbf{z}}\right)-b'_V\left({}^{n+1}\mathbf{z},\bar{\mathbf{z}}\right)\ \forall\bar{\mathbf{z}}\in Z \quad (53)$$

where

$$b^*_\Gamma\left({}^{n+1}\mathbf{z};\Delta\dot{\mathbf{z}},\bar{\mathbf{z}}\right)\equiv b^*_N\left({}^{n+1}\mathbf{z};\Delta\dot{\mathbf{z}},\bar{\mathbf{z}}\right)+b^*_T\left({}^{n+1}\mathbf{z};\Delta\dot{\mathbf{z}},\bar{\mathbf{z}}\right) \quad (54)$$

Since the left side of equation (53) is same as the left side of equation (42) if $\Delta\dot{\mathbf{z}}$ is replaced by $\Delta\mathbf{z}$, the design sensitivity equation uses the same stiffness matrix as response analysis that already has a factorized form. This provides an excellent efficiency in computation of design sensitivity.

Figure 7 shows the flow chart of response analysis and DSA. The response analysis is carried our using a meshfree code developed at Iowa. The response analysis of the stamping process involves elastoplasticity, finite deformation, and frictional contact of shell structure. For response analysis of a finite deformation elastoplastic shell structure, which corresponds to 'Compute Structural stiffness and Force' in Figure 7, the Hughes-Winget's incrementally objective integration with the elastoplastic return-mapping algorithm for shell structure is used. The detail discussion of response analysis and DSA can be found in Reference [13] for frictionless contact. The nonlinear response analysis is to find the equilibrium state corresponding to the applied loads. Time variable t is used to denote the intensities of load applications, or different punch location in stamping process, and correspondingly different configurations. The basic approach in nonlinear response analysis is to assume that the solution at time t is known and that the solution at time t+Δt is required, which is obtained based on the Newton-Raphson iteration method. After the solution is obtained, the DSA is performed with NDV number of design variables. In DSA, since the global stiffness matrix **K** is same as that in response analysis, the sensitivity calculation is carried out without iteration, which makes DSA very efficient.

6. NUMERICAL EXAMPLE

The S-rail benchmark problem of NUMISHEET'96 is selected in this paper to demonstrate the efficiency and accuracy of the proposed method for a stamping process

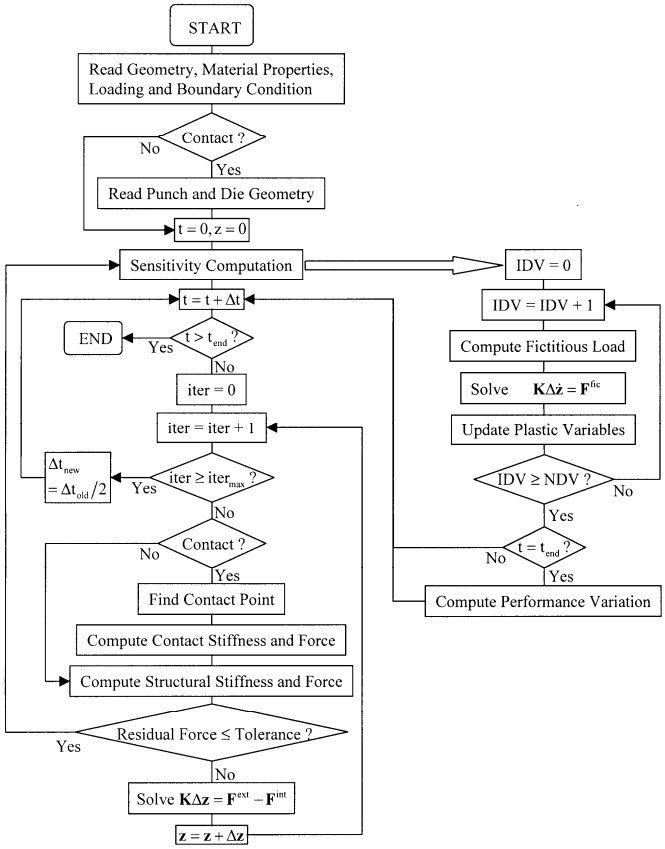

Figure 7. Flow Chart of Response Analysis and Design Sensitivity Analysis

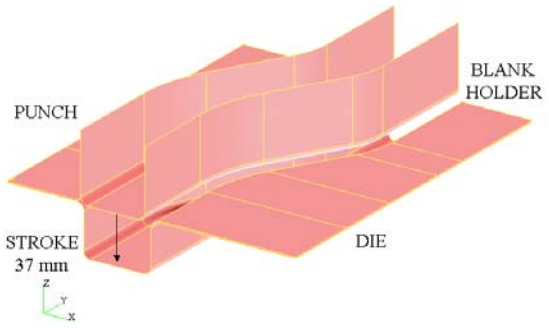

Figure 8. Schematic of S-rail Forming and Springback

optimization. As mentioned before, this is a quite challenging problem, even for accuracy of the analysis, let alone for DSA and optimization.

The blank sheet with thickness t=0.92 mm is placed on the die and hold by the blank holder with constant force 10 kN. Then the punch is pressed down with 37 mm stroke and removed. Due to elasticity, significant springback occurs. The material properties are Young's modulus E=69 GPa, Poisson's ratio ν=0.33, and the yield strength σ_Y=241 MPa. For elasto-plasticity, the combined linear isotropic-kinematic hardening rule is used with a hardening slope of H=200 MPa. The modified Coulomb friction law is used with a friction coefficient of 0.1. Figure 8 shows the tool surfaces for the S-rail forming process and Figure 9 shows the blank sheet.

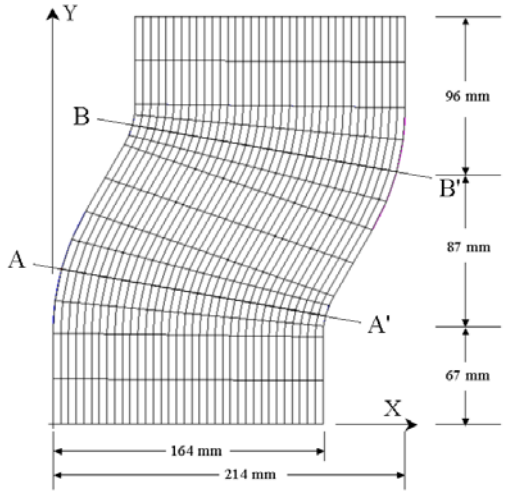

Figure 9. Blank Sheet of S-rail Forming and Springback

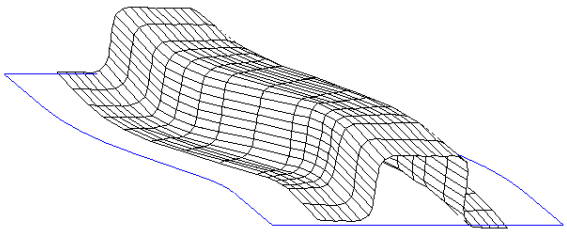

(a) Before Springback

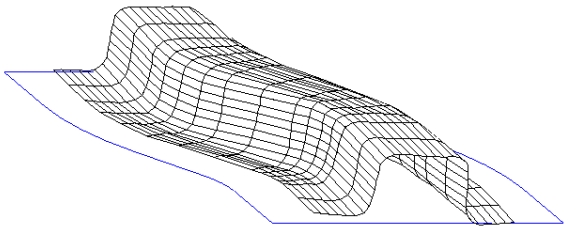

(b) After Springback

Figure 10. Deformed Shape

Since the die, punch, and blank holder are rigid, only blank sheet is discretized using 540 meshfree particles. In addition, the vertical displacement of the blank holder needs to be computed. Therefore, 2701 degrees-of-freedoms are used to model the stamping process. 200 time steps have been used to carry out the nonlinear analysis, which took 39908 seconds using a workstation with 1GHz Itanium CPU. Figures 10 (a) and (b) show deformed shapes before and after springback. In order to calculate the deformed shape after the tools are removed, one point is fixed to avoid rigid-body motion. For the shell element, fixing one point is enough since the rotational degrees of freedom is fixed too. The deformed shape along the line A-A′ on Figure 9 is shown in Figure 11, where significant springback has occurred. Thus, stamping process optimization is carried out to minimize the springback.

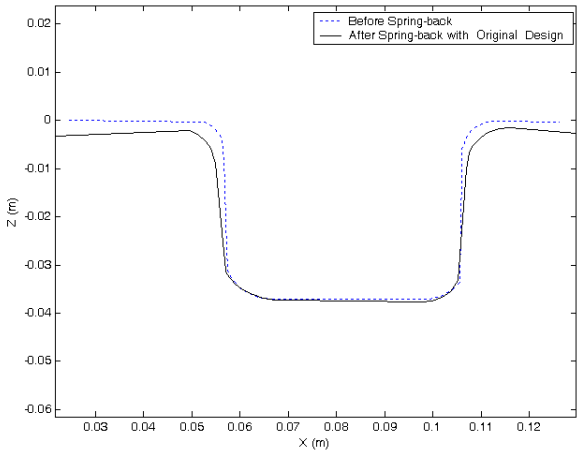

Figure 11. Deformed Shape along Line A-A′ Before and After Springback

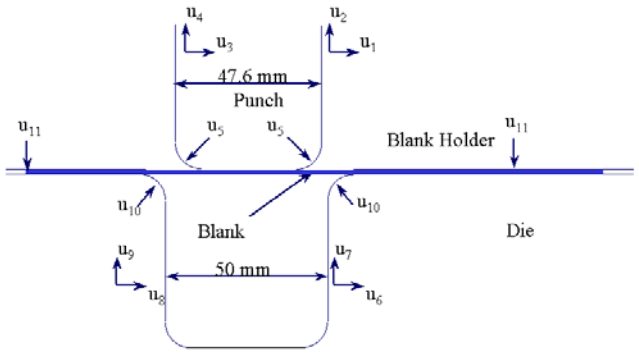

Figure 12. Shape and Configuration Parameters for S-rail Stamping Process

The stamping parameters are defined as shown in Figure 12. The stamping parameters u_1~u_4 represent the horizontal and vertical location of each side of punch and u_6~u_9 represent those of die. The stamping parameters u_5 and u_{10} represent

corner radius of punch and die respectively. The stamping parameter u_{11} represents the blank holding force. The computational time for the continuum-based sensitivity analysis per each stamping parameter is 2113 seconds, which corresponds to 5.3% of the response analysis time, and thus very efficient compared to the finite difference method. The accuracy of the sensitivity results of vertical displacements after springback along the lines A-A′ and B-B′ with respect to stamping parameter u_6 is compared with the finite difference results in Table 1. Extremely accurate sensitivity results are obtained, as shown in Table 1.

Table 1. Accuracy of design sensitivity results

Perf.	ψ	$\Delta\psi$	$\psi\times\Delta\tau$	$(\Delta\psi/\psi/\Delta\tau)$ $\times 100$
Z_{109}	-1.3555E-03	5.1913E-10	5.1989E-10	99.85
Z_{114}	-5.2567E-03	-3.2754E-09	-3.2873E-09	99.64
Z_{119}	-2.8827E-02	-3.2496E-09	-3.2619E-09	99.62
Z_{122}	-3.7159E-02	4.4464E-10	4.4617E-10	99.66
Z_{125}	-3.6658E-02	-3.2416E-10	-3.2346E-10	100.22
Z_{126}	-3.7233E-02	-5.0735E-10	-5.0659E-10	100.15
Z_{131}	-3.1223E-02	2.2928E-09	2.3064E-09	99.41
Z_{133}	-2.1987E-02	2.2657E-09	2.2798E-09	99.39
Z_{138}	-9.0185E-04	-2.4509E-10	-2.4106E-10	101.67
Z_{141}	-6.2609E-04	-1.1656E-09	-1.1672E-09	99.86
Z_{142}	-1.0870E-03	-3.4639E-10	-3.4813E-10	99.50
Z_{144}	-1.3831E-05	-1.5467E-10	-1.5505E-10	99.76

The stamping process optimization problem is formulated to minimize the springback as

$$
\begin{aligned}
\text{Min} \quad & \left(z_{144}^{\text{before\_sb}} - z_{144}^{\text{after\_sb}}\right) \\
\text{S.T.} \quad & \left(z_{109}^{\text{before\_sb}} - z_{109}^{\text{after\_sb}}\right) \le 0.0015 \\
& e^{p} \le 0.2 \\
-0.1 \le\ & u_1 \le 0.001 \\
-0.001 \le\ & u_2 \le 0.1 \\
-0.001 \le\ & u_3 \le 0.1 \\
-0.001 \le\ & u_4 \le 0.1 \\
-2.0 \le\ & u_5 \le 2.0 \\
-0.001 \le\ & u_6 \le 0.1 \\
-0.1 \le\ & u_7 \le 0.001 \\
-0.1 \le\ & u_8 \le 0.001 \\
-0.1 \le\ & u_9 \le 0.001 \\
-2.0 \le\ & u_{10} \le 2.0 \\
-2.0 \le\ & u_{11} \le 2.0
\end{aligned}
\qquad (55)
$$

where $z_{144}^{\text{before\_sb}}$ and $z_{144}^{\text{after\_sb}}$ are vertical displacements at the left end of the blank sheet in Figure 11 before and after springback, respectively. Similarly, $z_{109}^{\text{before\_sb}}$ and $z_{109}^{\text{after\_sb}}$ are vertical displacements at the right end of the blank sheet before and after springback, respectively. The initial values of $\left(z_{144}^{\text{before\_sb}} - z_{144}^{\text{before\_sb}}\right)$ and $\left(z_{109}^{\text{before\_sb}} - z_{109}^{\text{before\_sb}}\right)$ are 3.2 mm and 2.7 mm, respectively. Thus, the first constraint, which is imposed on the amount of springback at the right end of the blank sheet is violated significantly at the initial design of the manufacturing process. This optimization formulation was used, instead of trying to minimize the spring back at both ends simultaneously, since it converged better in the optimization process. The effective plastic strain constraints are imposed to limit the amount that may result in material failure or severe necking. The maximum effective plastic strain at the initial stamping process is 0.188, which makes the initial stamping process satisfy the effective plastic strain constraints. Limits of stamping parameters are established according to work piece geometry and kinematics. Since the stamping parameters represent structure's relative movements, the initial values are set to zero.

The stamping process optimization problem is solved using the sequential linear programming method in DOT by providing the meshfree analysis results and design sensitivity computed using the proposed method. As shown in Figure 13, the optimization problem is converged in six iterations, which is quite fast considering the degree of high nonlinearity involved in the structural analysis. The cost function, which is the spring back at the left end of the blank sheet, is reduced by 75% (from 3.2 mm to 0.8 mm) during the optimization. On the other hand, the springback at the right end of the blank sheet, which is the first constraint, is reduced significantly from 2.7 mm to 0.35 mm as shown in Figure 14. The effective plastic strain constraints are also satisfied. The design parameter history is given in Figure 15. It is noticed that the corner radius of the die, u_{10}, and the corner radius of the punch, u_5, are significantly reduced. It is also interesting to note that the blank holding force, u_{11}, is decreased from the initial design, which in turn reduces the frictional force. Unlike some optimum design results of linear models, it is not easy to explain why these optimum stamping process parameters yield minimized springback.

The deformed shape for the optimum manufacturing process is shown in Figure 16. Over deflection of the initial stamping process around the blank holder area is significantly reduced in order to minimize the springback that is shown in Figure 11. The vertical slope is also improved as compared to the initial stamping process.

7. CONCLUSION

A continuum-based design sensitivity analysis (DSA) method for the stamping process has been developed. Since the proposed DSA method uses the same tangent stiffness as the analysis at the converged configuration of each time step, no iteration is required to solve the sensitivity equation. Consequently, DSA takes much less computational time than the nonlinear response analysis. The sensitivity information is compared with finite difference results with excellent agreement. The effectiveness of the proposed continuum-based DSA method is demonstrated through optimization of the benchmark S-rail stamping process, where springback is

significantly reduced by determining optimal tool shape and blank holding force.

8. ACKNOWLEDGEMENT

This research is supported by a research grant from General Motors Corporation. This support is gratefully acknowledged.

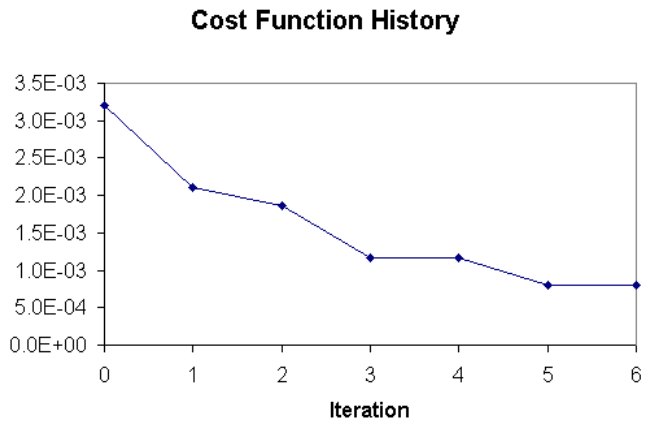

Figure 13. Cost Function History of S-rail Forming

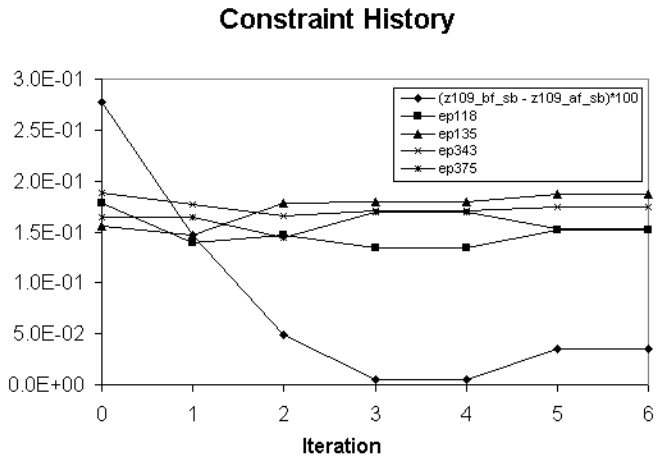

Figure 14. Constraint History of S-rail Forming

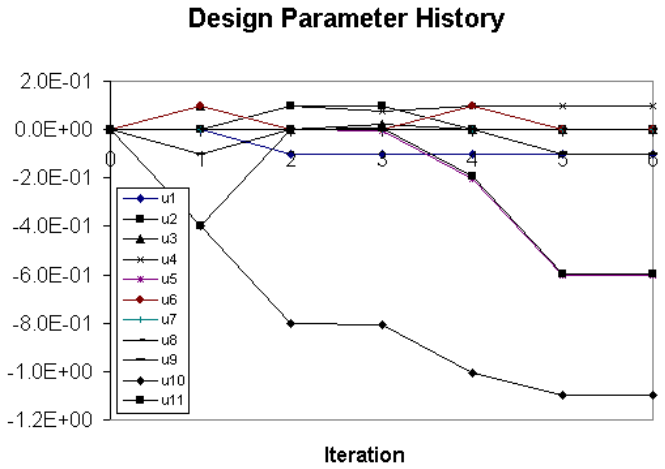

Figure 15. Design Parameter History of S-rail Forming

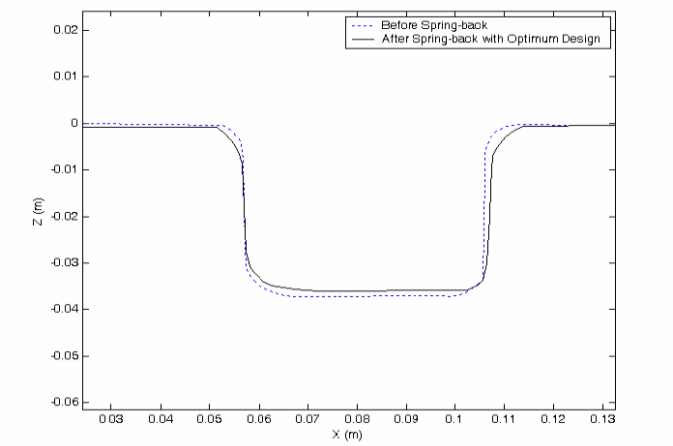

Figure 16. Deformed Shape along A-A′ Before and After Springback of the Optimum Stamping Process

9. REFERENCES

1. Yoon, J.W., Yang, D.Y., and Chung, K., “Elasto-plastic finite element method based on incremental deformation theory and continuum based shell elements for planar anisotropic sheet materials”, Computer Methods in Applied Mechanics and Engineering, Vol. 174, 23-56, 1999.
2. Yoon, J.W., Pourboghrat, F., Chung, K., Yang, D., “Spring-back prediction for sheet metal forming process using a 3D hybrid membrane/shell method”, International Journal of Mechanical Science, Vol. 44, 2133-2153, 2002.
3. Lee, M., Kim, D., Kim, C., Wenner, M.L., and Chung, K., “Spring-back evaluation of automotive sheets based on isotropic-kinematic hardening laws and non-quadratic anisotropic yield functions, Part III: Applications”, International Journal of Plasticity, Vol. 21, 915-953, 2005.

4. NUMISHEET'93 Organizing Committee, In: Makinouchi, A., Nakamachi, E., Onate, E., Wagoner, R.H.(Eds.), Proceedings of 2nd International Conference on Numerical Simulation of 3D Sheet Metal Forming Processes-Verification of Simulation with Experiment, Isehara, Japan, 1993.
5. NUMISHEET'96 Organizing Committee, In: Lee, J.K., Kinzel, G.L., Wagoner, R.H. (Eds.), Proceedings of Third Conference, Nuisheet'96, The Ohio State University, U.S.A., 1996.
6. NUMISHEET2002 Organizing Committee, In: Yang, D.Y., Oh, S.I., Huh, H., Kim, Y.H. (Eds.), Proceedings of 5th International Conference and Workshop on Numerical Simulation of 3D Sheet Forming Processes, Jeju, Korea., 2002.
7. Wenner, M.L., "On work hardening and springback in plane strain draw forming", Journal of Applied Metalworking, Vol. 2, 342-349, 1983.
8. Liu, Y.C., "The effect of restraining force on shape deviation in flanged channels," Journal of Engineering Materials and Technology, Vol. 110, 389-394, 1988.
9. Karafillis, A.P. and Boyce, M.C., "Tooling and binder design for sheet metal forming processes compensating springback error", International Journal of Machine Tools and Manufacturing, Vol. 36, 503-526, 1996.
10. Sosnowski, W., Marczewska, I., and Marczewski, A., "Sensitivity based optimization of sheet metal forming tools", Journal of Materials Processing Technology, Vol. 124, 319-328, 2002.
11. Yang, J., Jeon, B., and Oh, S., "Design sensitivity analysis and optimization of the hydroforming process," Journal of Materials Processing Technology, Vol. 113, 666-672, 2001.
12. Naceur, H., Guo, Y.Q., Batoz, J.L., and Knopf-Lenoir, C., "Optimization of drawbead restraining forces and drawbead design in sheet metal forming process", International Journal of Mechanical Sciences, Vol. 43, 2407-2434, 2001.
13. Choi, K.K., Yi, K., Kim, N-H., and Botkin, M.E., "Design Sensitivity Analysis of Nonlinear Shell Structure with Frictionless Contact," 29th ASME Design Automation Conference, *DETC2003/DAC-48795*, September 2-6, 2003, Chicago, IL.
14. Simo, J.C., Taylor, R.L., "A return mapping algorithm for plane stress elastoplasticity", International Journal of Numerical Methods in Engineering, Vol. 22, pp. 649-670, 1986.
15. Hughes, T.J.R. and Winget, J., "Finite rotation effects in numerical integration of rate constitutive equations arising in large deformation analysis", International Journal of Numerical Methods in Engineering, Vol. 15, pp. 1862-1867, 1980.
16. Hughes, T.J.R., "Numerical implementation of constitutive models: rate-independent deviatoric plasticity", *Theoretical Foundation for Large-scale Computations of Nonlinear Material Behavior*, Edited by Nemat-Nasser, S., Asaro, R.J., and Hegemier, G.A., Martinus Nijhoff Publishers, 1984.
17. Fish, J. and Shek, K, "Computational aspect of incrementally objective algorithms for large deformation plasticity", International Journal of Numerical Methods in Engineering, Vol. 44, pp. 839-851, 1999.
18. Chang, K.H., Choi, K.K., Tsai C.S., Chen, C.J., Choi, B.S., and Yu, X., "Design sensitivity analysis and optimization tool (DSO) for shape design applications", Computing Systems in Engineering, Vol. 6, 151-175, 1995.